Biomaterials 216 (2019) 119244

Contents lists available at ScienceDirect

Biomaterials

journal homepage: www.elsevier.com/locate/biomaterials

Microengineered human amniotic ectoderm tissue array for high-content developmental phenotyping

Sajedeh Nasr Esfahani[a,1], Yue Shao[a,d,1], Agnes M. Resto Irizarry[a], Zida Li[a,e], Xufeng Xue[a], Deborah L. Gumucio[b], Jianping Fu[a,b,c,*]

[a] Department of Mechanical Engineering, University of Michigan, Ann Arbor, MI, 48109, USA
[b] Department of Cell and Developmental Biology, University of Michigan Medical School, Ann Arbor, MI, 48109, USA
[c] Department of Biomedical Engineering, University of Michigan, Ann Arbor, MI, 48109, USA
[d] Koch Institute for Integrative Cancer Research, Massachusetts Institute of Technology, Cambridge, MA, 02142, USA
[e] Department of Biomedical Engineering, School of Medicine, Shenzhen University, Shenzhen, 518060, China

ARTICLE INFO

Keywords:
Human pluripotent stem cells
Lumenogenesis
Amniogenesis
Micropatterning
Teratogen
Drug screening

ABSTRACT

During early post-implantation human embryogenesis, the epiblast (EPI) within the blastocyst polarizes to generate a cyst with a central lumen. Cells at the uterine pole of the EPI cyst then undergo differentiation to form the amniotic ectoderm (AM), a tissue essential for further embryonic development. While the causes of early pregnancy failure are complex, improper lumenogenesis or amniogenesis of the EPI represent possible contributing factors. Here we report a novel AM microtissue array platform that allows quantitative phenotyping of lumenogenesis and amniogenesis of the EPI and demonstrate its potential application for embryonic toxicity profiling. Specifically, a human pluripotent stem cell (hPSC)-based amniogenic differentiation protocol was developed using a two-step micropatterning technique to generate a regular AM microtissue array with defined tissue sizes. A computer-assisted analysis pipeline was developed to automatically process imaging data and quantify morphological and biological features of AM microtissues. Analysis of the effects of cell density, cyst size and culture conditions revealed a clear connection between cyst size and amniogenesis of hPSC. Using this platform, we demonstrated that pharmacological inhibition of ROCK signaling, an essential mechanotransductive pathway, suppressed lumenogenesis but did not perturb amniogenic differentiation of hPSC, suggesting uncoupled regulatory mechanisms for AM morphogenesis *vs.* cytodifferentiation. The AM microtissue array was further applied to screen a panel of clinically relevant drugs, which successfully detected their differential teratogenecity. This work provides a technological platform for toxicological screening of clinically relevant drugs for their effects on lumenogenesis and amniogenesis during early human peri-implantation development, processes that have been previously inaccessible to study.

1. Introduction

During implantation of the human embryo, the epiblast (EPI) within the blastocyst polarizes to form a pluripotent cyst with a central lumen enclosing the pro-amniotic cavity [1,2]. Shortly thereafter, embryonic cells at the pole of the EPI cyst adjacent to the invading trophoblast lose pluripotency and differentiate into the squamous amniotic ectoderm (AM). The AM tissue will eventually develop into the amniotic membrane that encloses and protects the developing fetus [3,4]. The development of the AM is an important milestone in early human embryogenesis, as it supplies the early embryo with critical inductive as well as supportive signals for subsequent development [5]. It has been estimated that up to 50% of pregnancies fail in the first two weeks after gestation, the window in which lumenogenesis and amniogenesis of the EPI are played out [6–8]. Yet, these two embryogenic events are understudied, and currently there is no technological platform available for analysis of compounds or drugs that might perturb these two embryonic developmental processes. The drastic differences in timing and location of the AM development between human and mice also limit the use of the mouse model to predict potential drug toxicity on the lumenogenesis and amniogenesis of the EPI during early human peri-implantation development [3,9].

Human pluripotent stem cells (hPSC), including human embryonic stem cells (hESC) and induced pluripotent stem cells (hiPSC), have

* Corresponding author. Department of Mechanical Engineering, University of Michigan, Ann Arbor, MI, 48109, USA.
E-mail address: jpfu@umich.edu (J. Fu).
[1] These authors contributed equally to this work.

https://doi.org/10.1016/j.biomaterials.2019.119244
Received 14 April 2019; Accepted 1 June 2019
Available online 07 June 2019
0142-9612/

significant self-organizing properties and developmental potential that allow them to differentiate into any somatic cell types in the human body [10–13]. Recently, we have developed an *in vitro* model of peri-implantation lumenogenesis and amniogenesis of the EPI using hPSC in the context of a three-dimensional (3D) Geltrex culture system (Gel-3D culture) [14,15]. In this system, singly dissociated hPSC are plated on top of a thick Geltrex layer; 24 h later, a dilute Geltrex overlay is applied, to establish a 3D culture environment. Although the Gel-3D system is established in a defined biochemical condition conductive for hPSC self-renewal, hPSC in the Gel-3D culture spontaneously self-organize and develop into lumenal, human amnion-like cystic structures [14,15]. Although the Gel-3D platform can efficiently generate human AM tissues, it is not suitable for high-throughput drug and toxicological screening applications as individual amniotic cysts show significant variations in size and stages of development [14,15].

Here, we sought to leverage the self-organizing properties and differentiation potential of hPSC to develop an AM microtissue array platform that is controllable, scalable and compatible with high-content imaging, thus suitable for high-throughput screening applications. We first investigated the effects of initial culture parameters, including cell plating density and timing of 3D ECM overlay addition, on amniogenic differentiation of hPSC. This led to the development of a two-step micropatterning method, capable of generating a regular array of AM microtissues with controlled shapes and sizes for high-content toxicity profiling of drugs and small molecules for their potential effects on the lumenogenesis and amniogenesis of the EPI. A computer-assisted analysis pipeline, which could automatically process imaging data and quantitatively measure morphological and biological parameters of lumenal cystic structures, was developed to streamline the data analysis pipeline. To demonstrate a proof-of-concept application of the AM microtissue array for high-content developmental phenotyping, we investigated the effect of Y27632, a ROCK inhibitor, on multiple phenotypic parameters of hPSC lumenogenesis and amniogenesis. Furthermore, to demonstrate its application as a drug screening system, we applied the regular AM microtissue array to assess the differential teratogenic effects of a panel of six clinically relevant drugs, which successfully detected their differential teratogenecity.

2. Methods

2.1. Two-step micropatterning

A two-step micropatterning method was developed to print a regular array of adhesive islands with defined sizes and shapes using Geltrex (Thermo Fisher Scientific; derived from Engelbreth-HolmSwarm tumors similarly as Matrigel®) on coverslips. Briefly, a patterned elastomeric stamp, made of poly-dimethylsiloxane (PDMS) and containing an array of circular posts, was first generated using replica molding from a silicon mold fabricated by standard photolithography and deep reactive ion etching (DRIE), as described previously [16,17]. The center-to-center spacing between adjacent posts on the PDMS stamp was 150 μm, and the post height was 30 μm. Stamps containing circular posts with different diameters ranging from 30 μm to 100 μm were used in this work. PDMS stamps were first soaked in 1% Geltrex solution for 24 h at 4 °C, before being rinsed with distilled water and blown dry with nitrogen. A glass coverslip pre-coated with a thin layer of PDMS was then treated with ultraviolet (UV) ozone (UV-ozone cleaner; Jelight, Irvine, CA) for 7 min to oxidize the PDMS surface, changing the PDMS surface from hydrophobic to hydrophilic to allow transfer of Geltrex from the PDMS stamp to coverslips coated with PDMS. PDMS stamps were then placed in conformal contact with coverslips for about 5 s to transfer Geltrex from the stamps to coverslips. To prevent protein adsorption onto non-functionalized regions of coverslips, coverslips were then treated with pluronics F127 NF dissolved in PBS (0.2%, *w/v*; BASF, Ludwigshafen, Germany) for 1 h at room temperature followed by rinsing with distilled water. Coverslips were then immersed in mTeSR medium (STEMCELL Technologies) for at least 2 h followed by fresh mTeSR medium containing 1% Geltrex for another 1 h. Coverslips were washed with PBS before cell seeding.

2.2. Cell culture

H9 cells (WA09, WiCell; NIH registration number: 0062) were used in this study. All culture protocols have been pre-approved by the Human Pluripotent Stem Cell Research Oversight Committee at the University of Michigan. The H9 hESC line is authenticated by the original source, and further authenticated in house by immunostaining for pluripotency markers and differentiation into the three germ layers. Karyotype analysis was performed by Cell Line Genetics. The H9 hESC line was tested negative for mycoplasma contamination (LookOut Mycoplasma PCR Detection Kit, Sigma-Aldrich).

H9 cells were cultured in a feeder-free culture system using mTeSR1 medium and lactate dehydrogenase-elevating virus (LDEV)-free, hESC-qualified reduced growth factor basement membrane matrix Geltrex, per manufacturer's instructions. During each passage, cultures were visually examined to remove spontaneously differentiated, mesenchymal-like cells. All hESC used in this work had passage numbers less than P70.

2.3. 3D amniogenesis assay on a coverslip

Cultured hESC colonies were dissociated into single cells with Accutase (Sigma-Aldrich) at 37 °C for 10 min before the cells were centrifuged and re-suspended in mTeSR1 medium containing 10 μM ROCK inhibitor, Y27632 (Tocris), to avoid dissociation-induced apoptosis [18]. Coverslips pre-coated with a thin layer of PDMS were either uniformly coated with 1% Geltrex or printed with a regular array of circular Geltrex islands. To establish 3D ECM overlay, 2 h or 24 h after initial cell seeding, culture medium was changed to a fresh mTeSR1 medium containing 4% (*v/v*) Geltrex, which was then replenished daily thereafter. Y27632 was removed from culture medium at 24 h after initial cell plating (day 1).

2.4. Image analysis

Images were acquired using an Olympus 1X81 fluorescence microscope, equipped with a CSU-X1 spinning-disc unit (YOKOGAWA) and an EMCCD camera (iXon X3, Andor). Fluorescence images acquired from confocal microscopy were reconstructed in 3D using Imaris8.2 (Bitplane). To extract morphological and molecular features of lumenal cystic structures taken in the images, we developed an image analysis pipeline based on edge detection, closing operation, thresholding, binary hole filling, and region property measurement in SciPy library for Python (Python Software Foundation, DE) or Image Processing Toolbox in MATLAB (MathWorks, Inc., MA). Specifically, the centroid of each lumenal cyst was first determined based on the region property measurement for DAPI staining images. The resultant cyst centroid was then used to calculate the coordinates used for cropping each cyst out of DAPI staining images as well as other staining channels. To calculate normalized fluorescent intensity relative to DAPI staining, a binary mask was first generated through thresholding to determine regions of the nuclei. Intensity ratios of other fluorescence labeling of the same cyst to DAPI staining under this binary mask were calculated as normalized fluorescent intensities.

Morphological features were extracted based on edge detection combined with other standard image processing operations. Edge detection was first performed to generate an image of the outer edge before the whole cyst was filled up by the binary hole filling operation. The area and equivalent diameter of the cyst was then calculated based on region property measurements performed on this image. To measure lumenal cavity dimension within a cyst, the same edge detection operation was performed on the original image, before part of the outer

edge was removed to make the outer edge discontinuous. Instead of filling up the whole cyst, binary hole filling operation on this image was conducted to fill up only the lumenal cavity. Region property measurements were then performed, and the area and equivalent diameter of the lumenal cavity were calculated.

2.5. Immunocytochemistry

hESC were fixed in 4% paraformaldehyde (buffered in 1 × PBS) for 1 h and permeabilized in 0.1% SDS (sodium dodecyl sulfate, dissolved in PBS) solution for 30 min. Samples were then blocked in 2% goat serum (Thermo Fisher Scientific) at 4 °C for 24 h and then incubated with primary antibody solution at 4 °C for another 24 h. Cells were then labeled with goat-raised secondary antibodies (1:400) at 4 °C for another 24 h. Cell nuclei were stained with 4,6-diamino-2-phenylindole (DAPI; Invitrogen). Alexa-Fluor dye-conjugated wheat germ agglutinin (WGA; Thermo Fisher Scientific) was used as a pan-cell membrane marker. All primary antibodies, their sources, and dilutions are listed in Supplementary Table 1.

2.6. Real-time PCR analysis

To prepare samples for RNA isolation, they were first washed with DMEM/F12 to remove Geltrex overlay. Cells were then scraped from coverslip surfaces and subsequently spun down at 1,000 r.p.m. for 3 min in a conical tube. A RNeasy Micro Kit (QIAGEN) was used following manufacturer's instructions to isolate RNA from cell pellet. A NanoDrop 1000 spectrophotometer (Thermo Scientific) was utilized to determine RNA quality and quantity. Reverse transcription was performed following the iScript cDNA Synthesis Kit (Bio-Rad). Quantitect Sybr Green MasterMix (QIAGEN) was then used to perform qRT-PCR analysis. To quantify relative gene expression, the $2^{-\Delta Ct}$ method was used, and human GAPDH was considered as an internal control. All RT-PCR analyses were conducted with $n = 3$–5 biological replicates and 2–3 technical replicates for each condition. Primers used in this work includes: TFAP2A (forward: GCATATCCGTTCACGCCGAT, and reverse: GGGAGATTGACCTACAGTGCC), TFAP2B (forward: AGCAAATGTCAC GTTACTCACC, and reverse: TGTGCTGCCGGTTCAAATACT), GATA3 (forward: GCCCCTCATTAAGCCCAAG, and reverse: TTGTGGTGGTCT GACAGTTCG), and GAPDH (forward: CTCTGCTCCTCCTGTTCGAC, and reverse: TTAAAAGCAGCCCTGGTGAC).

2.7. Statistical analysis

All experiments were conducted with $n = 3$–5 biological replicates and repeated in $n > 3$ independent experiments. Statistical analysis was performed using Excel (Microsoft; https://www. microsoft.com). *P*-values were calculated using unpaired, two-sided Student's *t*-test.

3. Results

3.1. Characterize the parameter-dependence of amniogenesis in 3D culture

Recent studies have strongly supported the important roles of initial culture parameters, including cell plating density and cell cluster size, in pluripotent stem cell (PSC)-based developmental models [10–13,15,19–22]. Thus, we first sought to examine the effects of initial culture parameters on the amniogenesis of hPSC in a 3D culture system. H9 hESC were dissociated into single cells before being plated at different cell seeding densities (5,000–30,000 cells cm^{-2}) onto a coverslip spin coated with PDMS and a thin layer of 1% Geltrex (see **Methods**), in mTeSR1 medium supplemented with ROCK inhibitor Y27632. We designated the time of cell seeding as $t = 0$ h 3D Geltrex overlay was added 24 h after initial cell seeding (day 1 or $t = 24$ h; Fig. 1a), at which point Y27632 was removed from culture medium. At $t = 2$ h after plating, most hESC had spread out but remained as single cells regardless of initial cell seeding densities (Fig. 1d). Over time, hESC began to cluster and initiate lumenogenesis. By $t = 24$ h, it became evident that higher initial cell seeding density resulted in cell clusters with more cells and greater cell cluster areas (Fig. 1d–f).

Previously, we showed that cell plating density affects amnion fate determination [14,15]. Consistent with that, the immunofluorescence analysis of TFAP2A, an AM marker identified in our previous study [14], showed that at higher cell plating densities (*e.g.*, ≥10,000 cells cm^{-2}), most of the lumenal cysts at day 3 were made of tall, columnar epithelial cells with apico-basally elongated nuclei; all of these columnar epithelial cells were negative for TFAP2A (Fig. 1b) but positive for OCT4 (data not shown), suggesting their undifferentiated pluripotent state. However, when initial cell plating density was decreased to 5,000 cells cm^{-2}, 57 ± 12% of cysts formed on the coverslip at day 3 were enclosed by squamous epithelial cells containing laterally elongated cell nuclei showing strong nuclear staining for TFAP2A, suggesting that these cells had spontaneously differentiated into the AM fate (Fig. 1b&c). Together, these data show that initial cell plating density is an important factor that modulates both cyst size and efficiency of AM differentiation in the 3D amniogenesis assay on a coverslip, and lateral elongation of cell nuclei perpendicular to the apico-basal axis of the AM tissue is a distinct morphological feature associated with differentiated AM tissues compared with pluripotent EPI cysts.

Given that lumenogenesis precedes amniogenesis [1,2] both *in vivo* and *in vitro*, and it is stimulated by addition of the ECM overlay, we tested whether introducing the 3D environment earlier might modify the timing or efficiency of amniogenesis. To investigate this, we added 3D ECM overlay at $t = 2$ h or $t = 24$ h (Fig. 2a), respectively. Interestingly, at the same cell plating density of 10,000 cells cm^{-2}, spontaneous AM differentiation was significantly enhanced when 3D ECM overlay was added at $t = 2$ h instead of $t = 24$ h (Fig. 2b): 95.3 ± 2% and 8.1 ± 5% of luminal cysts were squamous AM cysts expressing TFAP2A, respectively (Fig. 2b&c). Consistently, the average number of cells in each cell cluster at $t = 24$ h was significantly less when 3D ECM overlay was added at $t = 2$ h *vs.* $t = 24$ h (4 ± 0.6 cells *vs.* 8 ± 1.0 cells; Fig. 2c). Supplementing 3D Geltrex overlay before $t = 2$ h led to significant cell death (data not shown), as it became difficult for single hESC to cluster and form proper cell-cell contacts to promote their survival. Further increasing initial cell seeding density to 30,000 cells cm^{-2} and adding 3D ECM overlay at $t = 2$ h reduced the percentage of TFAP2A + AM cysts in Gel-3D to about 13 ± 2.5% at day 3 (Fig. 2d). Altogether, these data on the parameter-dependence of amniogenesis in 3D culture establish that an initial cell seeding density of 10,000 cells cm^{-2} and early introduction of 3D ECM overlay at $t = 2$ h as optimal culture conditions for successful *in vitro* amniogenesis.

3.2. Development of a microengineered human AM tissue array

Tissue microarray is a powerful platform with nearly identical multicellular tissue structures for high-throughput screening applications [23,24]. Thus, we next sought to generate an AM microtissue array under above-discovered 3D culture condition. To this end, we developed a 2-step micropatterning method to print a regular array of Geltrex adhesive islands with defined sizes and shapes (Fig. 3a; see **Methods**) onto a coverslip. Specifically, a standard microcontact printing process was first applied to print circular Geltrex adhesive islands onto a coverslip pre-coated with a thin layer of PDMS. After blocking with mTeSR, which contains bovine serum albumin (BSA), the coverslip was soaked in a fresh mTeSR medium containing 1% Geltrex (Fig. 3a; see **Methods**). Without this Geltrex recoating step, attachment of singly dissociated hESCs onto Geltrex adhesive islands was poor (Fig. 3b&c).

We next compared attachment of singly dissociated hESC onto circular Geltrex adhesive islands of different diameters (30–100 μm) prepared from the standard microcontact printing method or the 2-step

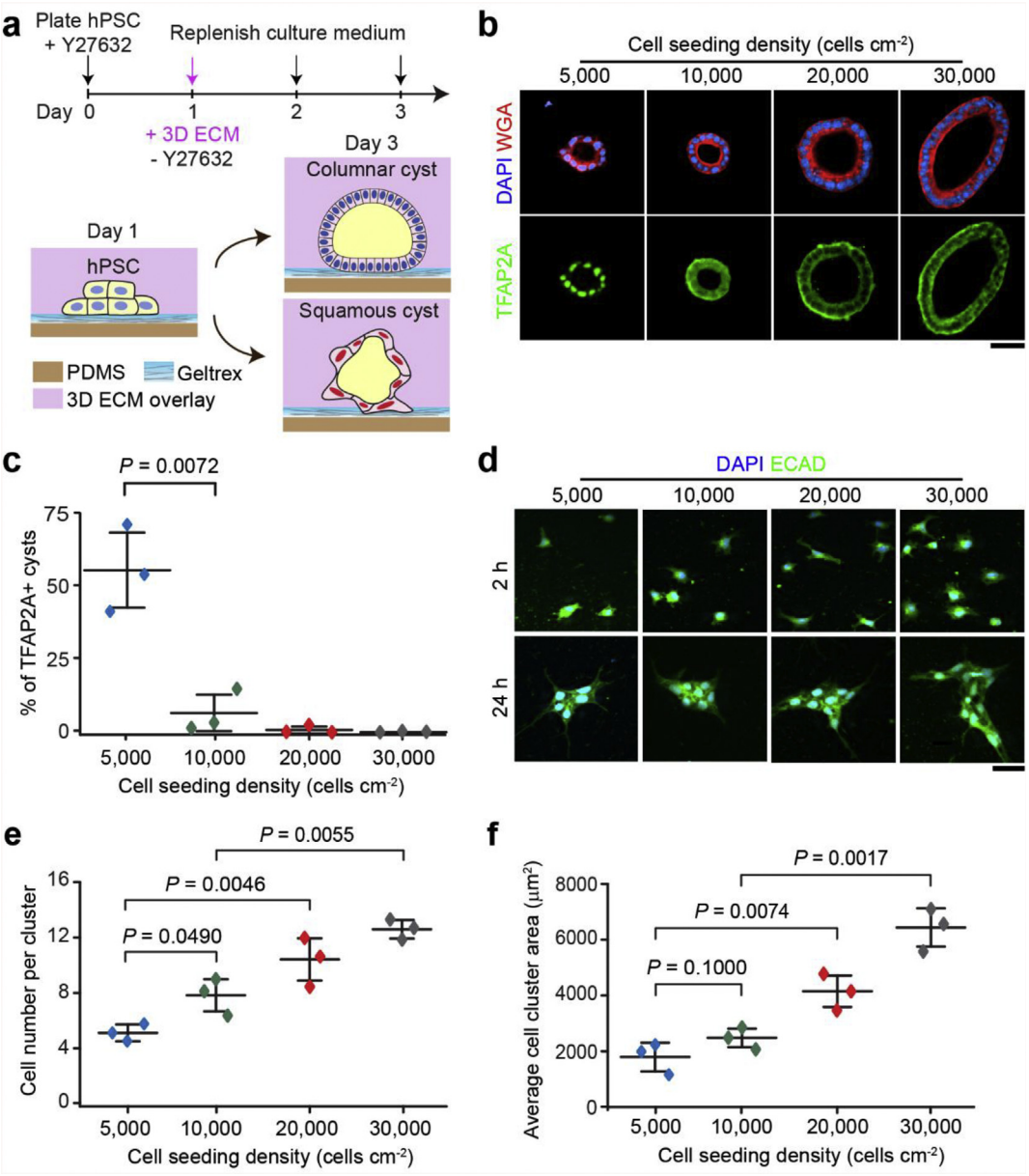

Fig. 1. Initial cell seeding density modulates AM differentiation. (a) Schematic showing hPSC differentiation to either columnar EPI or squamous amniotic cysts at day 3. As indicated, 3D ECM overlay was added 24 h after initial cell seeding. (b) Representative confocal micrographs showing cystic structures formed at day 3, stained for the membrane marker WGA (wheat germ agglutinin) and the amnion marker TFAP2A under different initial cell seeding density conditions as indicated. DAPI counterstains nuclei. (c) Plot showing percentages of TFAP2A + squamous amniotic cysts formed at day 3 as a function of initial cell seeding density. $n = 3$ independent experiments. Data represent the mean ± s.e.m. P value was calculated using unpaired, two-sided Student's t-test. (d) Representative immunofluorescence micrographs showing hPSC 2 h (top) or 24 h (bottom) after seeding under different initial cell plating density conditions as indicated. Cells were stained for E-cadherin (ECAD). DAPI counterstains nuclei. (e&f) Plots showing cell number per cell cluster (e) and average cell cluster area (f) as a function of initial cell seeding density. Cell clusters were imaged 24 h after cell seeding. $n = 3$ independent experiments. Data represent the mean ± s.e.m. P values were calculated using unpaired, two-sided Student's t-test. Scale bars in b & d, 50 μm.

micropatterning method. Consistent cell attachment improvement was observed for the 2-step micropatterning method for all adhesive island sizes tested (Fig. 3c). Additionally, as expected, the average number of hESC initially attached to circular Geltrex adhesive islands increased with increasing island diameter (Fig. 3c).

We next examined the effect of adhesive island diameter (from 30 to 100 μm) on AM microtissue development. To this end, singly dissociated hESC were seeded onto circular Geltrex adhesive islands with an initial cell seeding density of 30,000 cells cm^{-2}.3D ECM overlay was supplemented 2 h after initial cell seeding ($t = 2$ h). Circular Geltrex adhesive islands with a diameter ≤80 μm induced efficiently spontaneous formation of amniotic cystic tissues enclosing a single central lumen and expressing TFAP2A (Fig. 3d&e). However, when circular Geltrex adhesive islands were too small (*e.g.*, with a diameter of 30 μm), significant cell death was observed (Fig. 3d&e). Furthermore, islands with a diameter of 100 μm often led to formation of amniotic cystic structures containing multiple lumens or sometimes collapsed cysts (Fig. 3d). Altogether, our results in Fig. 3 suggest that a diameter of 80 μm for circular Geltrex adhesive islands is the optimal pattern size for the generation of a squamous AM microtissue array.

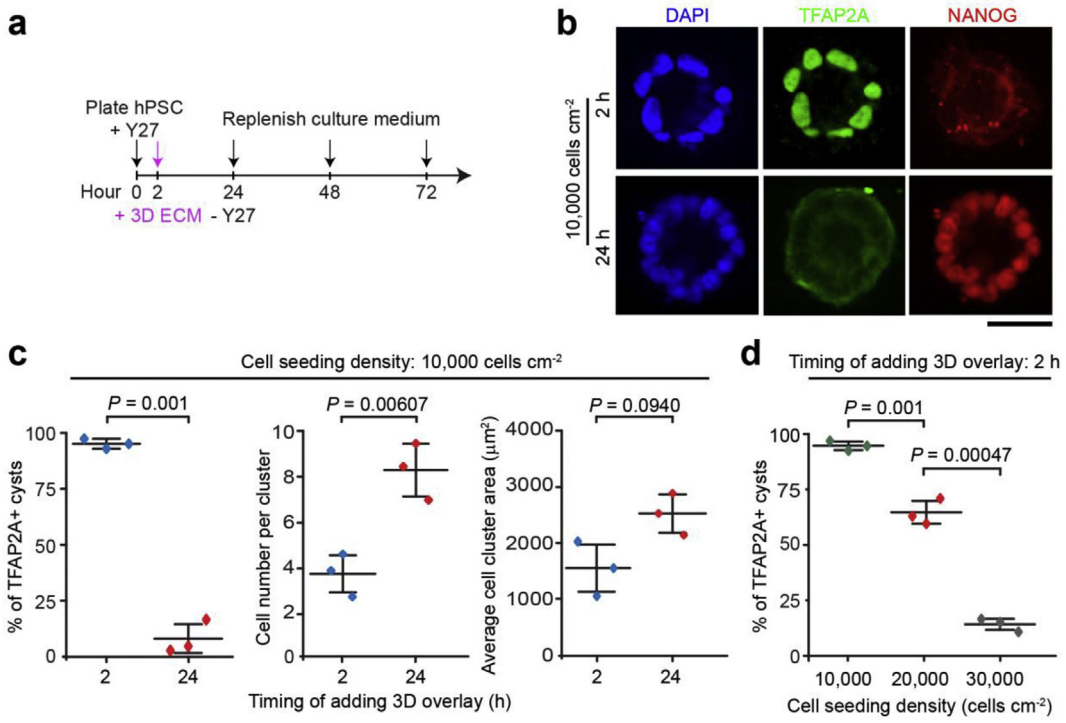

Fig. 2. Timing of adding 3D ECM overlay plays an important role in AM differentiation. (a) Schematic showing the hPSC amniotic differentiation protocol, in which 3D ECM overlay was added 2 h after initial cell seeding. (b) Representative confocal micrographs showing cystic structures formed at day 3 stained for TFAP2A and NANOG. DAPI counterstains nuclei. 3D ECM overlay was added either 2 h (top) or 24 h (bottom) after initial cell seeding at a density of 10,000 cells cm^{-2} as indicated. DAPI counterstains nuclei. Scale bar, 50 μm. (c) Left: Plot showing percentage of TFAP2A + amniotic cysts formed at day 3 as a function of the timing of adding 3D ECM overlay (2 h *vs.* 24 h after cell seeding). Middle and right: Plots showing cell number per cell cluster (middle) and average cell cluster area (right) for cell clusters imaged 24 h after cell seeding as a function of the timing of adding 3D ECM overlay (2 h *vs.* 24 h after cell seeding). Initial cell seeding density, 10,000 cells cm^{-2}. $n = 3$ independent experiments. Data represent the mean ± s.e.m. *P* values were calculated using unpaired, two-sided Student's *t*-test. (d) Plot showing percentage of TFAP2A + amniotic cysts formed at day 3 as a function of initial cell seeding density. 3D ECM overlay was added 2 h after cell seeding. $n = 3$ independent experiments. Data represent the mean ± s.e.m. *P* values were calculated using unpaired, two-sided Student's *t*-test.

3.3. Molecular characterization of squamous, hPSC-derived amnion-like tissue

To further examine the molecular signature of hPSC-derived AM tissues in the context of this microtissue array, cells were stained for markers that are highly upregulated during amniogenesis, including TFAP2A, GATA3 and TFAP2B [10,11], as well as pluripotency markers NANOG and SOX2, which are downregulated as cells exit the pluripotent state [10,11]. Positive nuclear staining of TFAP2A, GATA3 and TFAP2B and negative nuclear staining of NANOG and SOX2 were consistently evident in AM cystic tissues obtained after 3 days of culture (Fig. 4a). Furthermore, the amnion-like cystic tissues contained EZRIN + apical surfaces facing inward toward the cyst lumen, consistent with findings reported in our previous work (Fig. 4a) [10,11]. qRT-PCR analysis further confirmed upregulated gene expression of *TFAP2A*, *TFAP2B* and *GATA3* in AM cells compared to hESC (Fig. 4b).

3.4. Image analysis pipeline for high-content phenotyping of amniotic cystic tissues

One of the advantages of the microengineered AM microtissue array platform is that it can generate hundreds of uniform sized amniotic cysts on a single coverslip, providing a large number of amnion-like tissues for quantitative imaging analysis. To efficiently process imaging data, we developed an image processing program pipeline to quantitatively determine fluorescent intensity of molecular markers in amniotic cysts and their morphological features with minimal human intervention (Fig. 5a; see **Methods**). In brief, DAPI-stained images were used to locate cysts and generate cropped images of each cyst. The DAPI channel of cropped images was then utilized to generate masks, in order to isolate nuclear fluorescence output of different molecular markers. Normalized fluorescence intensity of these molecular markers was calculated as the ratio of the marker nuclear fluorescent intensity to DAPI fluorescence intensity. Morphological features of cystic structures were extracted through edge detection combined with other standard image processing operations to determine cyst inner and outer diameters and cyst wall thickness (Fig. 5a; see **Methods**).

To validate the image processing program pipeline and further demonstrate its application for the microengineered AM array, we first compared the average normalized fluorescent intensity of NANOG and TFAP2A at different time points during AM differentiation (Fig. 5b). Quantitative analysis revealed that NANOG intensity decreased significantly between day 1 and day 2, and but no significant change was detected between day 2 and day 3 (Fig. 5b). In contrast, TFAP2A intensity increased progressively from day 1 to day 3 (Fig. 5b). These observations suggest that hESC under the amniogenic environment begin to lose pluripotency and gain amniotic fate between day 1 and day 2; further amniogenic differentiation and lineage maturation continues from day 2 to day 3. Using the image processing program pipeline, we further compared columnar pluripotent cysts and squamous amniotic cysts in terms of molecular marker fluorescence intensities and cyst sizes. As expected, in hESC and columnar pluripotent cysts, the average normalized nuclear intensities of NANOG and TFAP2A are significantly higher and lower, respectively, than in squamous amniotic cysts (Fig. 5c). Additionally, on average, squamous amniotic cysts exhibit a significantly smaller diameter and cyst wall thickness compared to undifferentiated columnar pluripotent cysts (Fig. 5d).

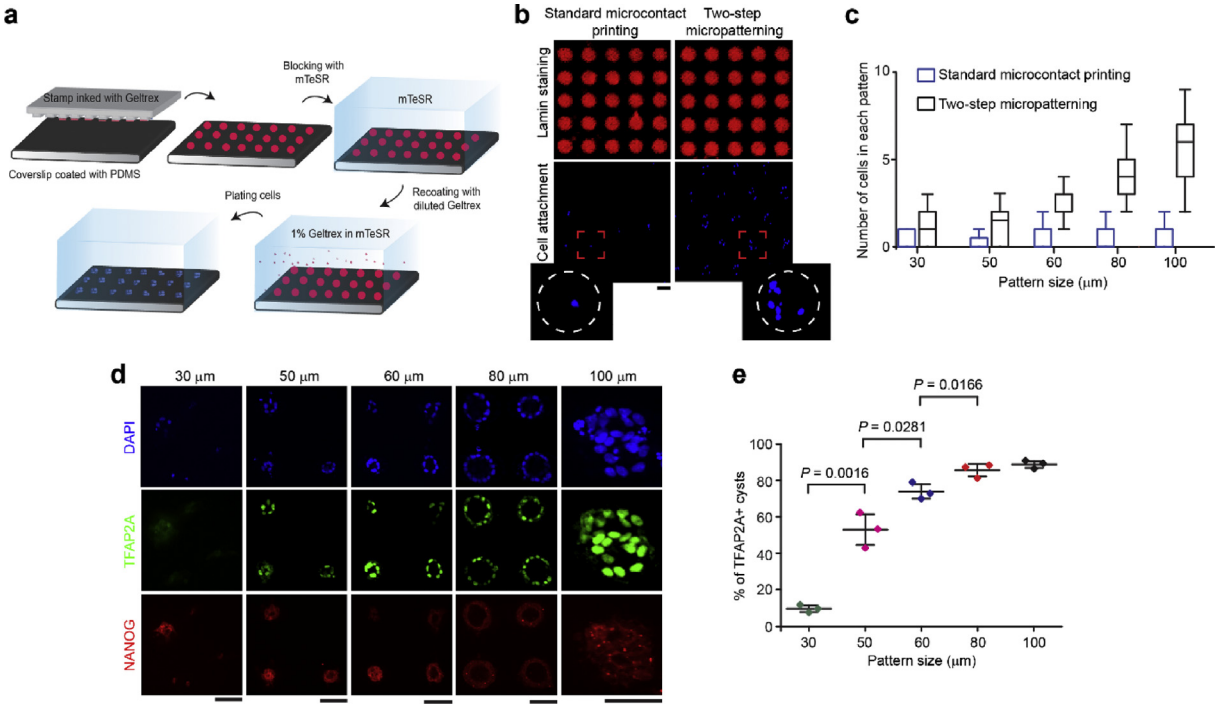

Fig. 3. A two-step micropatterning method to generate an AM tissue array. (a) Schematic showing the two-step micropatterning method to print an array of Geltrex coated adhesive islands on coverslips. (b) Representative immunofluorescence images showing hPSCs seeded onto arrays of Geltrex coated adhesive islands printed using the standard microcontact printing method (left) and the two-step micropatterning method (right). Samples were stained for laminin to visualize adhesive islands. DAPI counterstains nuclei. Samples were imaged 2 h after cell seeding. Zoom-in images show magnified views of individual adhesive islands. (c) Box chart of the average number of cells in individual adhesive islands as a function of island diameter. Box: 25–75%, bar-in-box: median, and whiskers: 1% and 99%. $n = 3$ independent experiments. Data from a total of 90 islands were pooled. (d) Confocal micrographs showing epithelial cysts formed at day 3 on adhesive islands of different sizes stained for TFAP2A and NANOG. DAPI counterstains nuclei. (e) Percentage of TFAP2A + cysts as a function of adhesive island diameter. $n = 3$ independent experiments. Data represent the mean ± s.e.m. P values were calculated using unpaired, two-sided Student's t-test. Scale bars in b & d, 50 μm.

3.5. Effect of ROCK inhibitor on AM cyst formation

The Rho-associated coiled protein kinase (ROCK)-dependent signaling pathway plays an important role in numerous physiological functions such as cell proliferation, adhesion, migration, and lumen formation [25,26]. Small molecule inhibitors of ROCK have been proposed for clinical uses in a variety of relatively common human diseases [27,28]. The microengineered AM microtissue array platform described here presents an opportunity to quantitatively investigate whether exposure to a ROCK inhibitor (Y27632) will affect differentiation or morphogenesis of lumenal AM cystic tissues. Here, in the drug treatment group cells were treated with Y27632 from day 0 to day 3, while in the control group Y27632 was removed from mTeSR medium at day 1. The concentration of Y27632 used in this study, which was 10 μM, is compatible to a recent study using Y27632 for glaucoma treatment in the monkey [28]. Immunostaining for TFAP2A, GATA3, TFAP2B and SOX2 was conducted at day 3 to identify AM cell fate. Quantitative analysis using the image processing program pipeline reveals no significant differences in the average normalized nuclear intensity of TFAP2A, GATA3, and TFAP2B between untreated control and Y27632-treated cells (Fig. 6a–d), supporting that interference with ROCK signaling does not perturb AM differentiation of hESC. However, cysts treated with Y27632 frequently displayed a flattened and collapsed morphology without a visible single, central lumen (Fig. 6e&f). Immunostaining for the apical marker EZRIN showed that Y27632 treatment resulted in clusters of amniotic cells with multiple EZRIN + lumens, in contrast with the control group, in which nearly all amniotic cysts had a single central lumen (Fig. 6g&h). Thus, ROCK signaling appears to play a critical role in lumenogenesis to form a central lumenal cavity, but not in amniotic fate determination of hESC.

3.6. Toxicological screening of clinically relevant drugs

To demonstrate the application of the microengineered AM microtissue array platform for teratogen screening, we selected a panel of six clinically relevant drugs and investigated their differential toxicity on the AM development. These drugs included: (1) Penicillin: a common antibiotic generally regarded as safe for pregnancy [29]; (2) Doxorubicin, a chemotherapy agent of pregnancy category D, which is known for its teratogenicity [30]; (3) Ibuprofen and Acetaminophen, two most commonly used over-the-counter painkillers. Acetaminophen, but not Ibuprofen, is recommended clinically for use during pregnancy [31,32]; (4) Dexamethasone and Citalopram, anti-inflammatory and anti-depressant, respectively, are two pregnancy category C drugs with undetermined toxicity on human embryo development.

In screening assays, cells were treated with each of these six drugs with a wide range of doses for a period of 3 d (Fig. 7 and Supplementary Figure 1). Concomitantly, cells in control groups were treated only with vehicles used for dissolving drugs. Cell viability was analyzed at day 3, with results normalized to control groups. The drug dose-response plots suggest that Penicillin has no detectable toxicity on the AM development, whereas Doxorubicin, as expected, induces massive cell death shortly after treatment (Fig. 7a&b). Interestingly, the toxicity, as measured by the median inhibitory concentration or IC50, of Acetaminophen and Ibuprofen showed a notable difference, with IC50 = 665 μM for Acetaminophen and IC50 = 202 μM for Ibuprofen, respectively (Fig. 7c&d and Table 1). This finding is consistent with empirical knowledge in the clinics that Acetaminophen, but not Ibuprofen, has negligible potential toxicity to the embryo and thus is recommended for use by pregnant women [31,33]. The anti-inflammatory drug Dexamethasone and the anti-depressant drug Citalopram showed much lower IC50 values compared with Ibuprofen

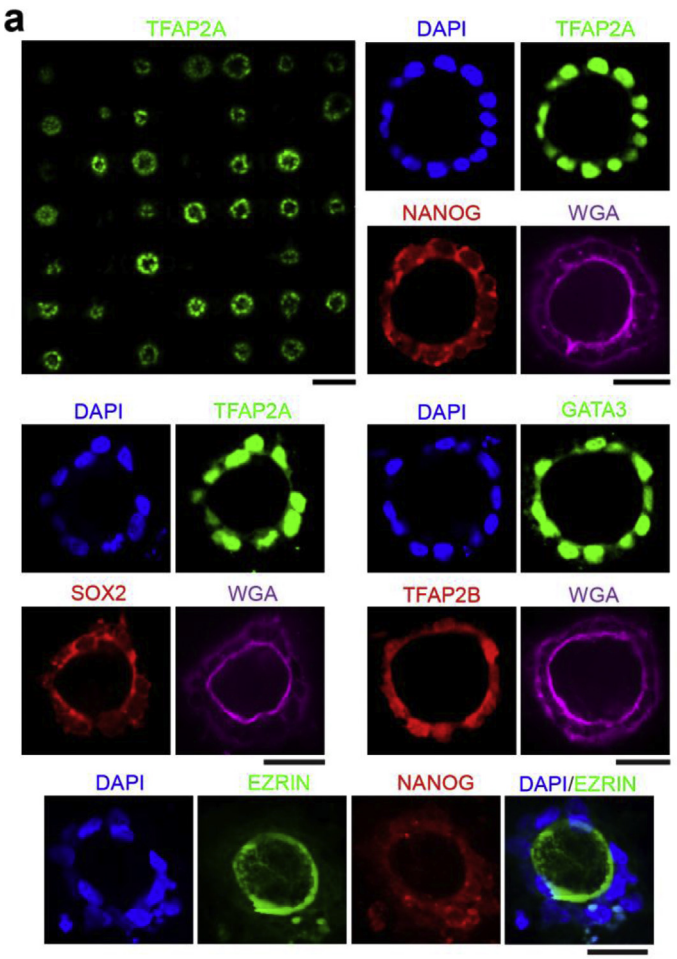

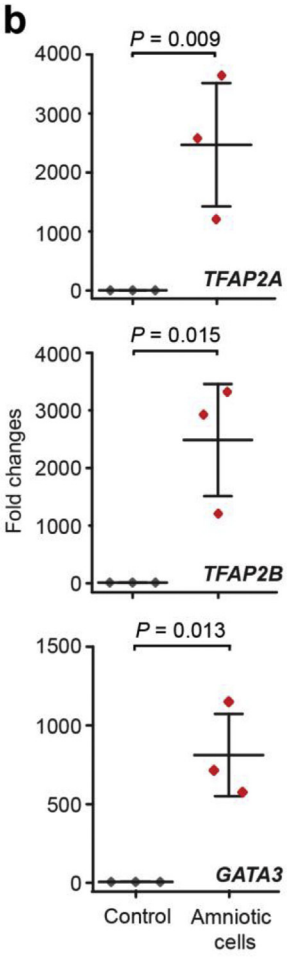

Fig. 4. Molecular characterization of squamous amniotic cysts. (a) Representative confocal micrographs showing AM microtissue array formed at day 3 on 80 μm diameter adhesive islands. Cells were stained for TFAP2A (top left), TFAP2A, NANOG and WGA (top right), TFAP2A, SOX2 and WGA (middle left), GATA3, TFAP2B and WGA (middle right), and EZRIN and NANOG (bottom). Scale bars, 50 μm. (b) Plot showing expression of *TFAP2A* (top), *TFAP2B* (middle), and *GATA3* (bottom) in hPSCs (control) and AM tissues. $n = 3$ independent experiments. Data represent the mean ± s.e.m. *P* values were calculated using unpaired, two-sided Student's *t*-test.

or Acetaminophen (Fig. 7e&f and Table 1), suggesting that these two drugs are potential human-specific teratogens for early embryonic development [34]. Together, these data demonstrate the microengineered AM microarray platform as a promising screening system to detect drug teratogenicity that aligns with clinical practice.

4. Discussion

Failure of embryonic implantation or development in the peri-implantation stage (within the first two weeks of pregnancy) is a common event, estimated to occur in up to 50% of pregnancies, often before the woman is aware of the pregnancy [6–8]. Pregnancy loss could be due to genetic or environmental causes, but neither the genes involved nor potential toxins that could contribute are known. Recently, we have reported an hPSC-based model that recapitulates peri-implantation human AM development [14,15]; here we leverage that model to generate a reproducible, standardized and scalable platform that can potentially be used to gain quantitative insight into both genetic and environmental factors that affect peri-implantation development.

Several recent reports highlight the important role of initial culture parameters, including cell plating density and cluster size, in PSC-based developmental models [9,11,17–22]. Our findings confirm a prominent role of both initial cell plating density and the timing of introducing 3D culture environment in the spontaneous development of AM cystic tissues from hPSC. Specifically, while high cell density in combination with addition of ECM overlay at 24 h did not elicit efficient amniogenesis, by either lowering cell seeding density or adding 3D ECM overlay 2 h, instead of 24 h, after initial cell seeding could rescue hPSC amniogenesis. Furthermore, the number of cells present in each cluster at the time of ECM addition affects the success of amniogenic differentiation as well: clusters with 1–2 cells typically die; clusters with 4–7 cells readily develop into AM cysts; while clusters with > 8 cells remain undifferentiated and generate columnar pluripotent EPI cysts. Together, these data show that while polarization and lumen formation can occur in hPSC with a broad range of cluster sizes, efficient acquisition of the AM fate occurs only within a narrow window of cyst sizes, suggesting that amniogenesis is linked to a community sensing mechanism [35]. A future goal is to elucidate how hPSC sense and respond to cluster size by activating the amniotic fate specification cascade.

Microcontact printing is one of the most commonly used methods to pattern different ECM proteins on cell culture surfaces [13,16,17,36]. In our hands, conventional microcontact printing was inadequate for printing Geltrex adhesive islands onto PDMS surfaces for efficient attachment of singly dissociated hPSC. This could be due to high sensitivity of Geltrex to temperature and premature gelation [37], which prevents efficient transfer of Geltrex to cell culture substrates. For this reason, we modified the conventional microcontact printing process by recoating patterned substrates with 1% Geltrex to improve hPSC attachment. Our data further show that with an initial cell seeding density of 30,000 cells cm^{-2}, a diameter of 80 μm for circular Geltrex adhesive islands is the optimal pattern size for the development of squamous AM microtissues containing a single central lumen. To efficiently process imaging data, a computer program-assisted image analysis pipeline was generated that could automatically process image data and measure morphological and biological parameters of luminal cysts including cyst size and molecular marker fluorescent intensity.

A proof-of-concept demonstration of the utility of the microengineered AM microtissue array platform for assessment of the effect

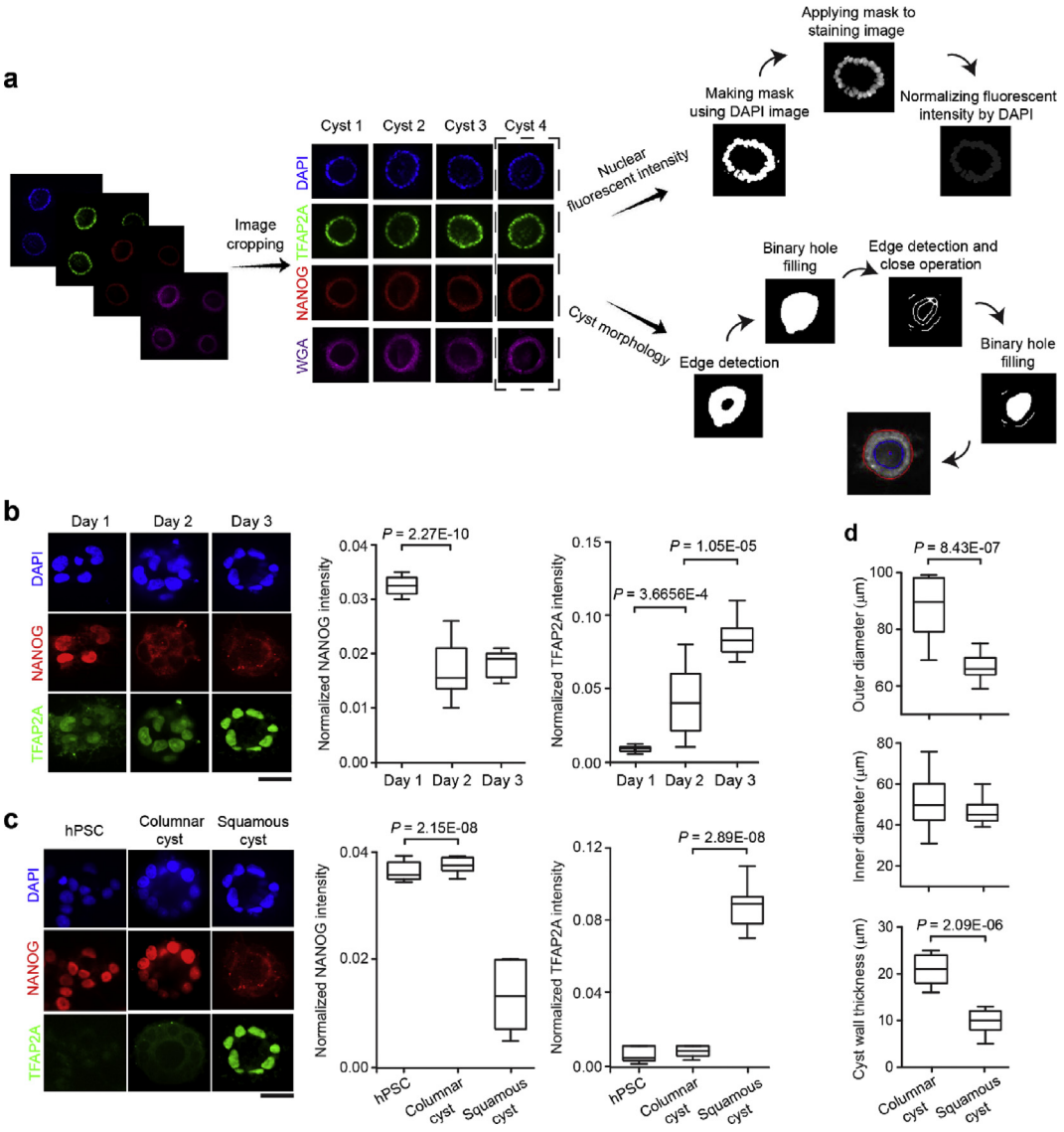

Fig. 5. Image analysis pipeline for high-content phenotyping of the AM microtissue array. (a) Image analysis pipeline schematic. (b) Dynamics of AM microtissue formation. Left: Representative confocal micrographs showing cells stained for NANOG and TFAP2A at different time points as indicated. DAPI counterstains nuclei. Right: Box charts showing average normalized NANOG and TFAP2A intensities as a function of time. Box: 25–75%, bar-in-box: median, and whiskers: 1% and 99%. $n = 3$ independent experiments. A total of 90 images were pooled and analyzed for each condition. *P* values were calculated using unpaired, two-sided Student's *t*-test. (c) Left: Representative confocal micrographs showing hPSC, columnar EPI cysts and squamous amniotic cysts at day 3 stained for NANOG and TFAP2A. DAPI counterstains nuclei. Right: Box charts showing average normalized NANOG and TFAP2A intensity in hPSC, columnar EPI cysts and squamous amniotic cysts as indicated. Box: 25–75%, bar-in-box: median, and whiskers: 1% and 99%. $n = 3$ independent experiments. A total of 90 images were pooled and analyzed for each condition. *P* values were calculated using unpaired, two-sided Student's *t*-test. (d) Box charts showing the outer diameter (top), inner diameter (middle), and cyst wall thickness (bottom) of columnar EPI cysts and squamous amniotic cysts formed at day 3. Box: 25–75%, bar-in-box: median, and whiskers: 1% and 99%. $n = 3$ independent experiments. A total of 90 images were pooled and analyzed for each condition. *P* values were calculated using unpaired, two-sided Student's *t*-test. Scale bars in b & c, 50 μm.

of small molecule drugs on early human peri-implantation development was further demonstrated by using Y27632, a ROCK inhibitor. This drug was chosen because a number of ROCK inhibitors have been approved by FDA and are either in use or proposed for use in clinical trials for common diseases (such as glaucoma and asthma) [27,28]. Women taking such drugs could be inadvertently exposing their early embryos to toxic insult if they are not yet aware that they are pregnant. Our data show that Y27632 treatment compromises lumenal morphogenesis in AM cysts, but interestingly, does not inhibit amniotic differentiation. Cysts treated with Y27632 often exhibited multiple lumens. This is consistent with previous studies on tubular lumen formation in epithelial organs [38,39], suggesting that proper formation of a single lumen depends on the ROCK-Myosin IIA pathway and that myosin IIA is essential for consolidating multiple lumens into a single lumen [40]. Alteration of the ROCK-Myosin IIA pathway also causes leaky tight junctions, which has been shown to prevent the consolidation of lumens in the developing zebrafish intestine [41]. The fact that even in cysts with multiple lumens, all cells differentiate uniformly to the AM is interesting and may rule out a role for mechanical forces emanating from a single central expanding lumen as a trigger for amniogenesis.

Because animal models are often associated with high costs and poor translation to humans [42,43], there is considerable interest in developing high-throughput, *in vitro* technologies to aid drug toxicity analysis [44–46]. To demonstrate the capacity of our platform as a teratogen screening system, we investigated dose-dependent toxicity of six clinically relevant drugs on the microengineered AM tissue array.

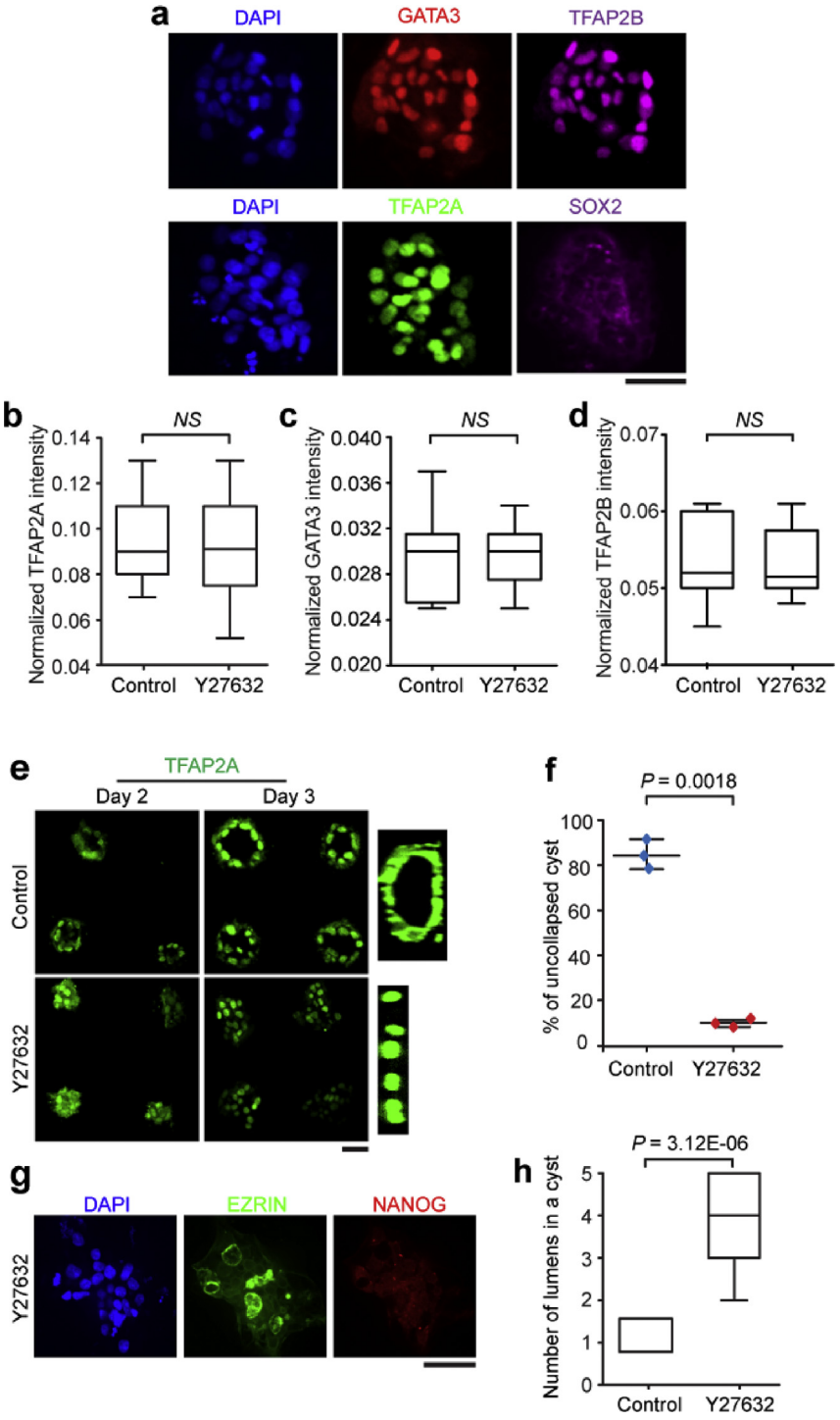

Fig. 6. Effect of ROCK inhibitor Y27632 on cyst morphology and amnion fate specification. (a) Representative confocal micrographs showing AM tissues formed at day 3 from hPSC treated with Y27632. Cells were stained for GATA3 and TFAP2B (top) or TFAP2A and SOX2 (bottom). DAPI counterstains nuclei. (b-d) Box charts showing average normalized TFAP2A (b), GATA3 (c) and TFAP2B (d) intensity in AM tissues formed at day 3 without (control) or with Y27632 treatments. Box: 25–75%, bar-in-box: median, and whiskers: 1% and 99%. $n = 3$ independent experiments. A total of 90 images were pooled and analyzed for each condition. P values were calculated using unpaired, two-sided Student's t-test. *NS*, statistically not significant and $P > 0.05$. (e) Confocal micrographs showing AM cells at day 2 and day 3 without (control) or with Y27632 treatments. Cells were stained for TFAP2A. Images on the right were x-z plane cross-sectional views. (f) Plot showing percentage of uncollapsed amniotic cysts formed at day 3 without (control) or with Y27632 treatment. Data represent the mean ± s.e.m. $n = 3$ independent experiments. P values were calculated using unpaired, two-sided Student's t-test. (g) Representative confocal micrographs showing AM tissues formed at day 3 with Y27632 treatment, stained for EZRIN and NANOG. (h) Box chart showing the average number of lumens in each cyst formed at day 3 without (control) or with Y27632 treatments. Box: 25–75%, bar-in-box: median, and whiskers: 1% and 99%. $n = 3$ independent experiments. A total of 90 images were pooled and analyzed for each condition. P values were calculated using unpaired, two-sided Student's t-test. Scale bars in a, e & f, 50 μm.

Importantly, our data correctly distinguished the differential teratogenic properties of Acetaminophen *vs.* Ibuprofen, two most commonly used painkillers. Specifically, our data supported that Acetaminophen has lower toxicity compared with Ibuprofen on AM tissues, which is consistent with the empirical knowledge in the clinical practice that Acetaminophen, but not Ibuprofen, is recommended to pregnant women [31,33]. In addition, our data substantiate evidence-based cautions when considering Dexamethasone and Citalopram, a common anti-inflammatory agent and a common anti-depressant drug, respectively, for use in pregnant women, echoing previous report in animal studies [34].

In summary, we have demonstrated for the first time an AM microtissue array platform from hPSC, which can generate uniform sized AM microtissues in an array format and is useful for peri-implantation drug toxicity screening. Our work is complementary to recently described platforms for high-throughput screening of chemicals that affect other developmental systems such as human embryonic vascular development or human neural progenitor cells [47,48]. We have further integrated this microtissue platform with a computer program-assisted image analysis pipeline to enable automatic, high-content profiling of morphological and biological parameters of AM microtissues developed under different conditions and drug perturbations. We envision that this microengineered AM microtissue array platform could be applied in the future to quantitatively compare

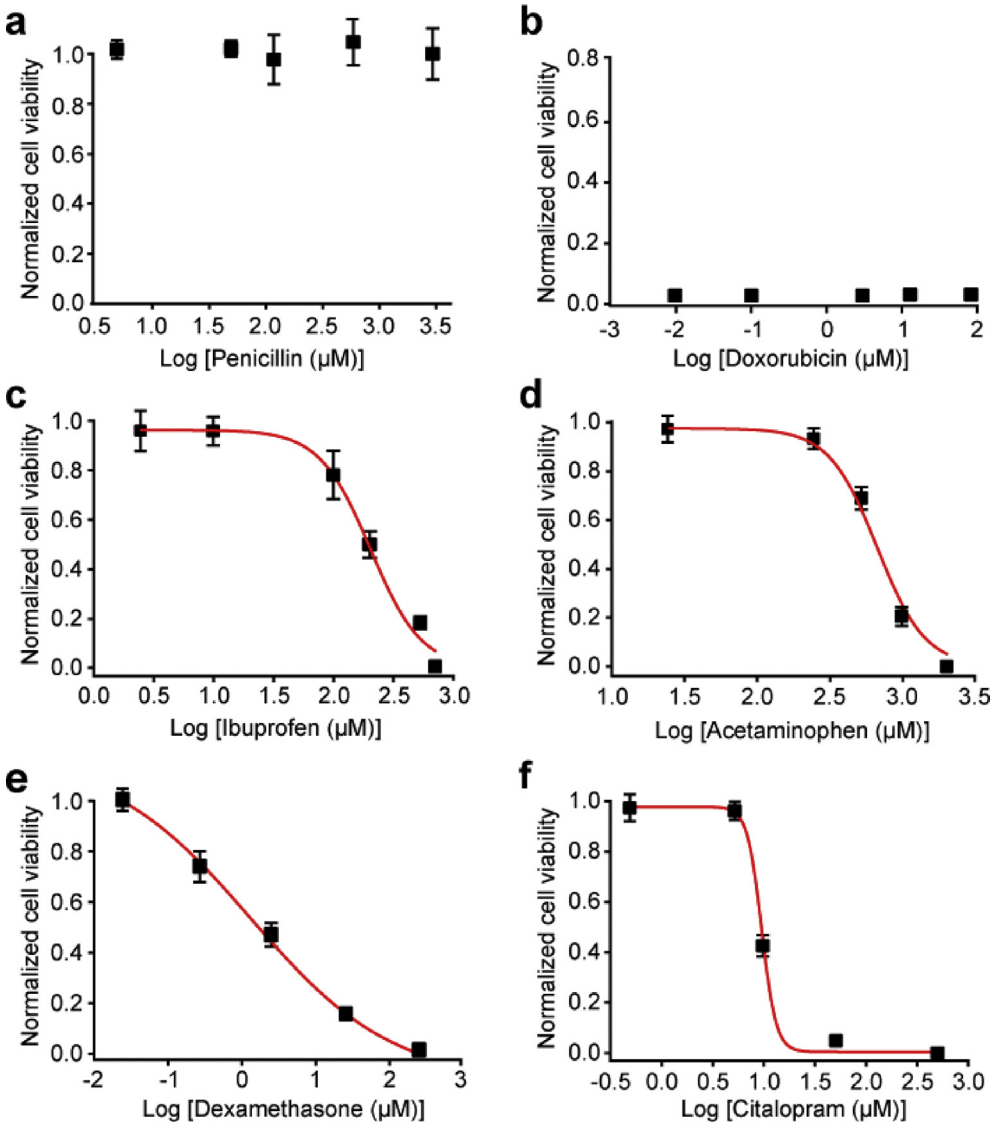

Fig. 7. Dose-dependent toxicity of clinically relevant drugs (a: Penicillin; b: Doxorubicin; c: Ibuprofen; d: Acetaminophen; e: Dexamethasone; f: Citalopram) on the development of AM microtissues. Data are plotted as the mean ± SEM for each concentration as determined from $n = 4$ independent experiments. Sigmoidal fits are plotted as solid lines.

Table 1
IC_{50} values of different drugs tested in Fig. 7. Dose-dependent toxicity data not amenable to sigmoidal fitting are represented as a dash in the table.

No.	Drug name	Clinical use	Log (IC50 ± SEM)	IC50 (μM)
1	Dexamethasone	Anti-inflammation	0.056 ± 0.126	1.136 ± 0.347
2	Citalopram	Anti-depression	0.977 ± 0.085	9.53 ± 1.834
3	Ibuprofen	Pain killer	2.30 ± 0.079	202.74 ± 36.76
4	Penicillin	Antibiotics	–	–
5	Doxorubicin	Chemotherapy drugs	–	–
6	Acetaminophen	Pain killer	2.81 ± 0.019	665.04 ± 28.60

lumenogenesis and amniogenesis in hPSC generated from infertile couples, or to test genetically manipulated hPSC for their ability to undergo these morphological and fate developments. Altogether, this microengineered AM microtissue array platform allows reproducible, scalable quantitative analysis of early human peri-implantation events that have been previously inaccessible to study.

Data availability

Data supporting the findings of this study are available within the article and its Supplementary Information files and from the corresponding author upon reasonable request.

Acknowledgments

This work is supported in part by the National Science Foundation (CMMI 1129611 and CBET 1149401, JF), the National Institutes of Health (DK089933, DLG), the National Science Foundation Graduate Research Fellowship under Grant No. DGE 1256260 (AMRI), and the Department of Mechanical Engineering at the University of Michigan. The Lurie Nanofabrication Facility at the University of Michigan, a member of the National Nanotechnology Infrastructure Network funded by the National Science Foundation, is acknowledged for support in microfabrication.

Appendix A. Supplementary data

Supplementary data to this article can be found online at https://

doi.org/10.1016/j.biomaterials.2019.119244.

References

[1] J. Rossant, P.P.L. Tam, Exploring early human embryo development, Science 360 (2018) 1075–1076.
[2] M.N. Shahbazi, M. Zernicka-Goetz, Deconstructing and reconstructing the mouse and human early embryo, Nat. Cell Biol. 20 (2018) 878–887.
[3] M.P. Dobreva, P.N. Pereira, J. Deprest, A. Zwijsen, On the origin of amniotic stem cells: Of mice and men, Int. J. Dev. Biol. 54 (2010) 761–777.
[4] W.P. Luckett, The development of primordial and definitive amniotic cavities in early Rhesus monkey and human embryos, Dev. Dynam. 144 (1975) 149–167.
[5] K. Sasaki, et al., The germ cell fate of cynomolgus monkeys is specified in the nascent amnion, Dev. Cell 39 (2016) 169–185.
[6] E.R. Norwitz, D.J. Schust, S.J. Fisher, Implantation and the survival of early pregnancy, N. Engl. J. Med. 345 (2001) 1400–1408.
[7] N.S. Macklon, J. Geraedts, B.C.J.M. Fauser, Conception to ongoing pregnancy: The 'black box' of early pregnancy loss, Hum. Reprod. Update 8 (2002) 333–343.
[8] E. Jauniaux, G.J. Burton, Pathophysiology of histological changes in early pregnancy loss, Placenta 26 (2005) 114–123.
[9] K. Ferner, A. Mess, Evolution and development of fetal membranes and placentation in amniote vertebrates, Respir. Physiol. Neurobiol. 178 (2011) 39–50.
[10] S.C. van den Brink, et al., Symmetry breaking, germ layer specification and axial organisation in aggregates of mouse embryonic stem cells, Development 141 (2014) 4231–4242.
[11] A. Warmflash, B. Sorre, F. Etoc, E.D. Siggia, A.H. Brivanlou, A method to recapitulate early embryonic spatial patterning in human embryonic stem cells, Nat. Methods 11 (2014) 847–854.
[12] M. Tewary, et al., A stepwise model of reaction-diffusion and positional-information governs self-organized human peri-gastrulation-like patterning, Development 144 (2017) 4298–4312.
[13] X. Xue, et al., Mechanics-guided embryonic patterning of neuroectoderm tissue from human pluripotent stem cells, Nat. Mater. 17 (2018) 633–641.
[14] Y. Shao, et al., Self-organized amniogenesis by human pluripotent stem cells in a biomimetic implantation-like niche, Nat. Mater. 16 (2017) 419.
[15] Y. Shao, et al., A pluripotent stem cell-based model for post-implantation human amniotic sac development, Nat. Commun. 8 (2017) 208.
[16] J. Fu, et al., Mechanical regulation of cell function with geometrically modulated elastomeric substrates, Nat. Methods 7 (2010) 733.
[17] S. Weng, Y. Shao, W. Chen, J. Fu, Mechanosensitive subcellular rheostasis drives emergent single-cell mechanical homeostasis, Nat. Mater. 15 (2016) 961–967.
[18] K. Watanabe, et al., A ROCK inhibitor permits survival of dissociated human embryonic stem cells, Nat. Biotechnol. 25 (2007) 681.
[19] T. Nakano, et al., Self-formation of optic cups and storable stratified neural retina from human ESCs, Cell Stem Cell 10 (2012) 771–785.
[20] M.A. Lancaster, et al., Cerebral organoids model human brain development and microcephaly, Nature 501 (2013) 373.
[21] M. Takasato, et al., Kidney organoids from human iPS cells contain multiple lineages and model human nephrogenesis, Nature 526 (2015) 564.
[22] L. Beccari, et al., Multi-axial self-organization properties of mouse embryonic stem cells into gastruloids, Nature 562 (2018) 272–276.
[23] Y. Shao, J. Fu, Integrated micro/nanoengineered functional biomaterials for cell mechanics and mechanobiology: A materials perspective, Adv. Mater. 26 (2014) 1494–1533.
[24] Y. Shao, J. Sang, J. Fu, On human pluripotent stem cell control: The rise of 3D bioengineering and mechanobiology, Biomaterials 52 (2015) 26–43.
[25] K. Taniguchi, et al., Lumen formation is an intrinsic property of isolated human pluripotent stem cells, Stem Cell Reports 5 (2015) 954–962.
[26] K. Gauthaman, C.-Y. Fong, A. Bongso, Effect of ROCK inhibitor Y-27632 on normal and variant human embryonic stem cells (hESCs) in vitro: Its benefits in hESC expansion, Stem Cell Reviews and Reports 6 (2010) 86–95.
[27] I. Sulaiman, J.C.W. Lim, H.L. Soo, J. Stanslas, Molecularly targeted therapies for asthma: Current development, challenges and potential clinical translation, Pulm. Pharmacol. Therapeut. 40 (2016) 52–68.
[28] N. Okumura, et al., Rho kinase inhibitor enables cell-based therapy for corneal endothelial dysfunction, Sci. Rep. 6 (2016) 26113.
[29] G.G. Nahum, K. Uhl, D.L.J.O. Kennedy, Gynecology, Antibiotic use in pregnancy and lactation: What is and is not known about teratogenic and toxic risks, 107 (2006) 1120–1138.
[30] K.K. Leslie, C. Koil, W.F.J.O. Rayburn, G. Clinics, Chemotherapeutic drugs in pregnancy 32 (2005) 627–640.
[31] S.L. Peters, et al., Safe Lists for Medications in Pregnancy: Inadequate Evidence Base and Inconsistent Guidance from Web-based Information vol. 22, (2011), pp. 324–328 2013.
[32] W.F. Hansen, A.E. Peacock, J. J. J. o. m. Yankowitz, w. s. health, Safe prescribing practices in pregnancy and lactation, 47 (2002) 409–421.
[33] K. Nezvalová-Henriksen, O. Spigset, Nordeng H. J. B. A. I. J. o. O, Gynaecology, Effects of ibuprofen, diclofenac, naproxen, and piroxicam on the course of pregnancy and pregnancy outcome: A prospective cohort study, 120 (2013) 948–959.
[34] X. Cheng, G. Wang, K. Ka Ho Lee, X. J. C. p. d. Yang, Dexamethasone use during pregnancy: Potential adverse effects on embryonic skeletogenesis, 20 (2014) 5430–5437.
[35] J.B. Gurdon, A community effect in animal development, Nature 336 (1988) 772.
[36] R. McBeath, D.M. Pirone, C.M. Nelson, K. Bhadriraju, C.S. Chen, Cell shape, cytoskeletal tension, and RhoA regulate stem cell lineage commitment, Dev. Cell 6 (2004) 483–495.
[37] P.T. Lieu, Reprogramming of human fibroblasts with non-integrating RNA virus on feeder-free or xeno-free conditions, Methods Mol. Biol. 1330 (2015) 47–54.
[38] B. Lubarsky, M.A. Krasnow, Tube morphogenesis, Cell 112 (2003) 19–28.
[39] E. Rodriguez-Boulan, I.G. Macara, Organization and execution of the epithelial polarity programme, Nat. Rev. Mol. Cell Biol. 15 (2014) 225–242.
[40] M. Kim, A. Shewan, A.J. Ewald, Z. Werb, K.E. Mostov, P114RhoGEF governs cell motility and lumen formation during tubulogenesis via ROCK-myosin II pathway, J. Cell Sci. 128 (2015) 4317–4327.
[41] M. Bagnat, I.D. Cheung, K.E. Mostov, D.Y. Stainier, Genetic control of single lumen formation in the zebrafish gut, Nat. Cell Biol. 9 (2007) 954.
[42] J.A. DiMasi, R.W. Hansen, Grabowski H. G. J. J. o. h. e, The Price of Innovation: New Estimates of Drug Development Costs vol. 22, (2003), pp. 151–185.
[43] M. Hay, D.W. Thomas, J.L. Craighead, C. Economides, J. Rosenthal, Clinical development success rates for investigational drugs, Nat. Biotechnol. 32 (2014) 40.
[44] S.N. Bhatia, D.E. Ingber, Microfluidic organs-on-chips, Nat. Biotechnol. 32 (2014) 760.
[45] J. El-Ali, P.K. Sorger, K.F. Jensen, Cells on chips, Nature 442 (2006) 403.
[46] J. Xing, Y.-C. Toh, S. Xu, H. Yu, A method for human teratogen detection by geometrically confined cell differentiation and migration, Sci. Rep. 5 (2015) 10038.
[47] H. Vazão, et al., High-throughput identification of small molecules that affect human embryonic vascular development, Proc. Natl. Acad. Sci. Unit. States Am. 114 (2017) E3022–E3031.
[48] G.J. Nierode, et al., High-throughput toxicity and phenotypic screening of 3D human neural progenitor cell cultures on a microarray chip platform, Stem cell reports 7 (2016) 970–982.